Article:

Liu, X., Tao, X., Liu, C. et al. (2 more authors) (2020) Investigation on the nanostructure of as-deposited and post-coat annealed CrCuAgN PVD nanocomposite coatings. Materials Chemistry and Physics, 255. 123499. ISSN 0254-0584

https://doi.org/10.1016/j.matchemphys.2020.123499

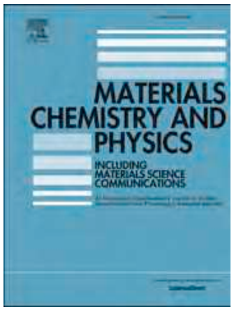

Investigation on the nanostructure of as-deposited and post-coat annealed CrCuAgN PVD nanocomposite coatings

Xingguang Liu, Xiao Tao, Chang Liu, Allan Matthews, Adrian Leyland

PII: S0254-0584(20)30864-6

DOI: https://doi.org/10.1016/j.matchemphys.2020.123499

Reference: MAC 123499

To appear in: *Materials Chemistry and Physics*

Received Date: 17 April 2020

Revised Date: 23 June 2020

Accepted Date: 28 June 2020

Please cite this article as: X. Liu, X. Tao, C. Liu, A. Matthews, A. Leyland, Investigation on the nanostructure of as-deposited and post-coat annealed CrCuAgN PVD nanocomposite coatings, *Materials Chemistry and Physics* (2020), doi: https://doi.org/10.1016/j.matchemphys.2020.123499.

Investigation on the nanostructure of as-deposited and post-coat annealed CrCuAgN PVD nanocomposite Coatings

Xingguang Liu[1,2*], Xiao Tao[2,3], Chang Liu[2], Allan Matthews[4] and Adrian Leyland[3]

[1] Science and Technology on Vacuum Technology Physics Laboratory, Lanzhou Institute of Physics, Lanzhou, 730000, China.
[2] Department of Materials Science and Engineering, The University of Sheffield, Sheffield, S1 3JD, United Kingdom.
[3] School of metallurgy and materials, University of Birmingham, Birmingham, B15 2TT, United Kingdom.
[4] School of Materials, The University of Manchester, Manchester, M13 9PL, United Kingdom.

[*] Corresponding author,
Full address: Lanzhou Institute of Physics, No. 100 Feiyan Street, Chengguan district, Lanzhou, Gansu Province, 730010, P.R. China.
Email: xingguangliu1@gmail.com;
Phone: +86-151-1721-7528

Highlights

1. CrCuAgN coatings with a wide range of Cu and Ag contents were prepared for investigation on their transport behavior.
2. The aggregation of both Cu and Ag are found to be detachment-limited, rather than diffusion-limited.
3. Cu was found to be beneficial in promoting Ag transport, resulting from the much higher detachment rate of Cu.
4. For the Cr-Cu-Ag-N system, coatings with desired specific nanostructures can be obtained via coating/process design.

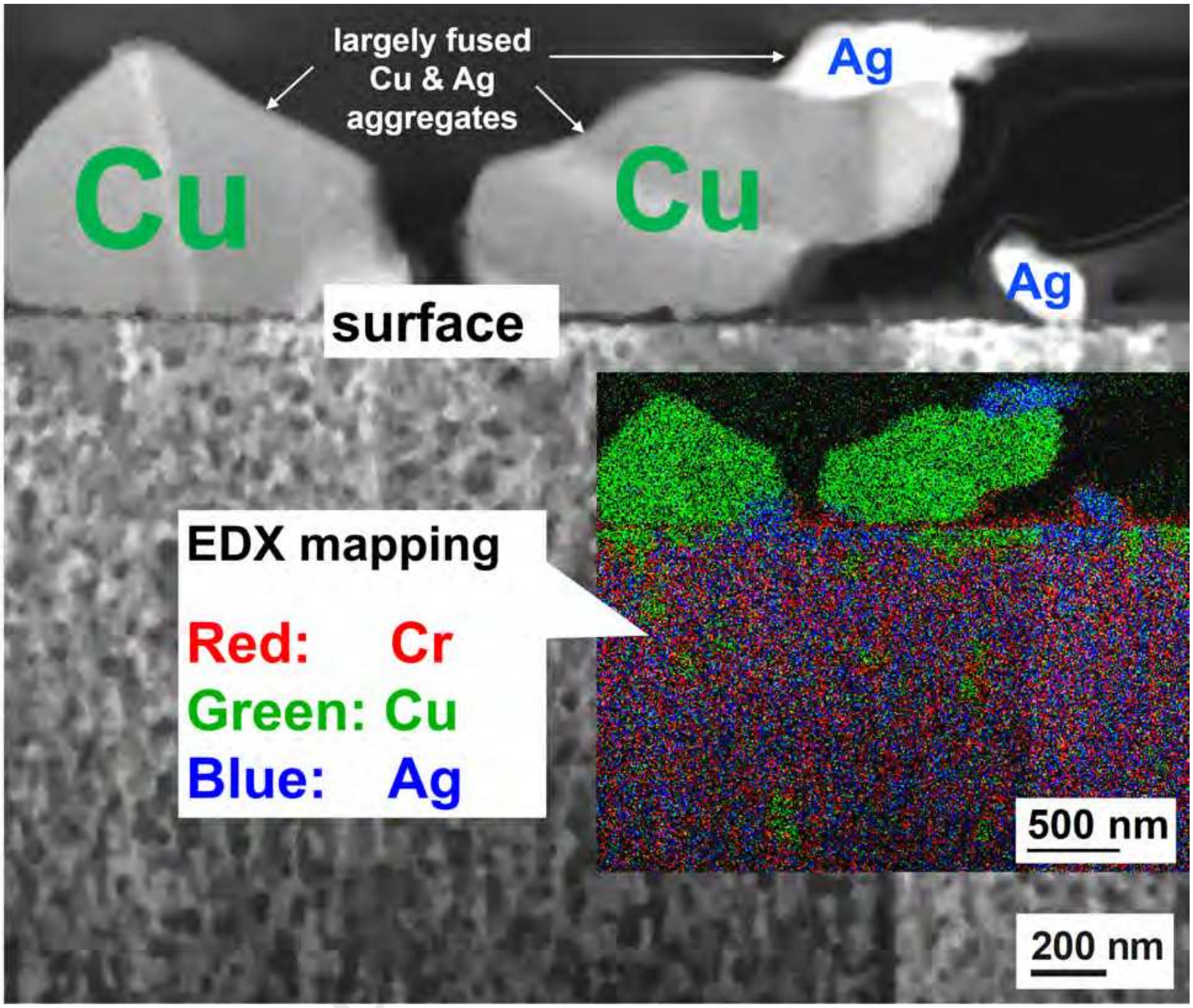
largely fused
Cu & Ag
aggregates
Ag
Cu
Cu
Ag
surface
EDX mapping
Red: Cr
Green: Cu
Blue: Ag
500 nm
200 nm

Investigation on the nanostructure of as-deposited and post-coat annealed CrCuAgN PVD nanocomposite coatings

Abstract

CrCuAgN coatings with a wide range of Cu and Ag contents (combined values in the range of <10 at% to >50 at%) were prepared on AISI316L stainless steel coupons by closed-field unbalanced magnetron sputtering(CFUBMS). After the deposition process, the coated coupons were annealed at 300 ℃ and 500 ℃, respect ively. The transport behaviour of Cu and Ag in selected CrCuAgN coatings was then investigated by conventional and high-resolution transmission electron microscopy (HR/TEM), energy-filtered (EF)TEM elemental mapping, and scanning (S)TEM with EDX elemental mapping. Results showed that the aggregation of both Cu and Ag are detachment-limited, rather than diffusion-limited. The co-existence of Cu with Ag in a PVD metallic coating was found to be beneficial in promoting Ag transport to the coating surface, resulting not from the anticipated "intergranular network channels" of Cu, but from a much higher detachment rate of Cu than Ag. This study verified that CrCuAgN coatings with desired composition and nanostructure can be obtained via coating/process design, providing controllable precipitation rate of Ag (via adjusting Cu content) for practical applications.

Keywords

PVD, Nanostructure, Cr-Cu-Ag-N quaternary system, Post-coat annealing, Transport

1. Introduction

PVD nanocomposite coatings containing ductile metals (e.g. Cu, Ag, etc.), as a solid-lubricating phases, embedded in a hard wear-resistant matrix such as a transition metal nitride [1-7], carbide [8, 9] or oxide [10-12], and mixtures of these ceramic phases (in ternary/quaternary nanocomposite coating systems), have been attracting increasing research interest for more than a decade. Some combinations exhibit promising tribological performance for applications which involve transient and/or cyclic temperature changes [13-15], as well as good antimicrobial [16-21] and anti-biofouling [22-24] performance. Particularly, composite coatings based on two typical ternary systems, Cr-Ag-N [5, 6, 13-15, 25, 26] and Cr-Cu-N [4, 16, 27], have taken their places in the research field of self-lubricating coatings. For the Cr-Ag-N system, it is found that Ag tends to exist as discrete, lamellar-shaped precipitates (height/width: ~ 1/2 to 1/3), distributed uniformly in the nitride matrix [28, 29]. The Cr-Cu-N system, however, is inclined to present two other different structures. Specifically, at low deposition temperatures [30] (typically ≤ 200 ℃), and low nitrogen content, Cu tends to exist in a bcc Cr matrix (yet with Cu-rich concentrations of up to 60 at.%), forming a metastable solid solution. At higher deposition temperatures (typically ≥ 200 ℃), and/or high nitrogen content Cu mainly ex ist in a semi-continuous Cu-rich intergranular 'tissue', surrounding nanocrystalline bcc Cr grains (or Cr nitrides if nitrogen is introduced, such as Cr_2N, CrN, or their mixture) [31, 32]. Furthermore, in regard to solid-lubricating and antimicrobial properties, Ag surpasses Cu, although Cu is generally considered better for anti-biofouling. One possible reason is that Ag is hardly (if not never) used to prevent marine biofouling, due to its much higher cost. Moreover, the use of Cu is in any case of concern because of 'danger' to marine life (i.e. high toxicity of Cu to fish and aquatic materials). However, the "dot" or "chain"-like distribution of Ag coating nanoparticles makes it more difficult for in-service replenishment supply to the coating surface, which is necessary for continuous and prolonged functionality. Fortunately, the “net”-like intergranular distribution of Cu in Cr-Cu-N coating systems offers a possible solution: i.e. to utilise intergranular Cu-rich phases as “transportation channels” for Ag. In other words, the Cr-Cu-Ag-N quaternary system is worthy of detailed study, for the purpose of combining the advantages (i.e. the efficient distributional structure of Cu and the more effective functionality of Ag) found in each of the abovementioned ternary systems (i.e. Cr-Cu-N and Cr-Ag-N).

In a previous study [17], the effect of post-coat annealing (at 300 ℃ and 500 ℃, respectively) on the surface morphology, phase composition and nanostructure of CrCuAgN coatings was investigated. Results showed that, with concentrations up to 16 at.%, N merely exists as a supersaturated interstitial solid solution in metallic Cr, with this solid solution being maintained even after a 2-hour post-coat anneal at 500 ℃. With sufficient Cu content however (e.g. > 12 at.%), annealing at such moderately high temperatures caused co-transportation of both Cu and Ag (even at relatively low Ag concentrations of ≤ 3 at.%) from inside the coating to the coating surface, creating a solid lubricant effect that significantly reduced the friction coefficient (CoF) when sliding against alumina or diamond. Specifically, for each counterface, a CoF reduction of >50% was observed, compared to those of the non-coated AISI 316L steel substrates. These results gave strong indication that the newly proposed Cr-Cu-Ag-N quaternary system is promising in temperature-dependent applications requiring ‘self-replenishment’. However, the CrCuAgN coatings in this previous study all contained relatively low Ag concentration (i.e. ~3 at.%), which provided limited applications-specific information, and a wider view of the Cr-Cu-Ag-N system is thus required for an in-depth understanding of its capabilities and potential. Therefore, further study of CrCuAgN coatings with, in particular, higher Ag concentrations is required.

The purpose of the present study therefore, was to investigate CrCuAgN coatings with a larger range of both Cu and Ag concentrations (e.g. Cu: ~5 to ~50 at.%; Ag: ~2 to 40 at.%), with combined values in the range of <10 at% to > 50 at%, in order to obtain a broader view of Cr-Cu-Ag-N PVD coating system performance in relation to nanostructures obtained, as well as further investigations of the annealing-induced transportation behaviour of both Cu and Ag. By doing so, we anticipated that clearer guidelines could be drawn for the design of CrCuAgN coatings for solid-lubricating and/or antimicrobial/antifouling applications.

2. Experimental

4 Cr, 1 Cu and 1 Ag small rectangular plates, all in dimensions of 130mm×100mm×6mm, were used to construct two 3-piece segmented targets, namely a Cr-Cr-Cu and a Cr-Cr-Ag target, as shown in Fig. 1. The interfacial angles between each target and the substrate holder (i.e. parallel to the coated substrate surface) are both 45° (see Fig. 1a). 9 mirror-finish AISI 316L stainless steel coupons of dimensions 50 mm × 25 mm × 2 mm were arranged into a 3 × 3 matrix, as shown in Fig. 1a, so as to obtain a series of coatings with varying elemental compositions but similar thicknesses.

The coating chamber was first pumped to a vacuum level of better than 2×10^{-5} mbar (2×10^{-3} Pa). Before the coating process, mirror polished AISI 316L stainless steel coupons (i.e. substrates) were sputter cleaned for 15 mins by an argon plasma (argon pressure: 3.3 Pa), generated by a substrate bias voltage of -700V via the attached sample holder. Then the argon pressure was reduced to 0.27Pa, for the following target sputter cleaning and deposition processes. After the target cleaning process, a ~200nm thick nitrogen-free CrCuAg interlayer was deposited on the substrates before the deposition of CrCuAgN coatings, in order to enhance the coating-substrate adhesion. Then Nitrogen was introduced at an increasing rate of 1 sccm/min [17, 33] until the final set value of 5 sccm was reached. Following the interlayer deposition process, a fixed nitrogen flow rate of 5 sccm was used for the deposition process of CrCuAgN coatings, in order to maintain the metallic states of these coatings. Namely, metallic nitrogen-containing chromium (being in majority proportion, if not entirely) rather than Cr nitride (based on results of the previous study [17]). A fixed power of 700W was applied to both segmented targets, making a total power of 1400 W, in accordance with the total target powers of the previous studies [17, 33]. The polished AISI 316L coupons, as substrates, were biased at a DC pulsed voltage of -100V, with substrate current densities being ~0.4 mA/cm^2. The total deposition duration was set to be 95 mins (including the deposition time of the interlayer), in order to keep a constant total deposition duration with our previous studies [17, 33].

Such CrCuAgN coatings were then annealed in a vacuum annealing furnace for a fixed duration of 2 hours, at two different annealing temperature, i.e. 300 ℃ and 500 ℃, respectively. Another set of as-deposited samples were reserved as the control group. The chamber for the annealing process was first pumped down to a vacuum level of better than 2.0 × 10^{-3} Pa, and the heated from room temperature at a rate of ~15 ℃/min. After the annealing temperature was reached (i.e. 300 ℃ or 5 00 ℃), the vacuum chamber was then held for two hours, with the annealing temperature fluctuation being within ±5 ℃. The chamber was then left under vacuum overnight for cooling back to room temperature. The nanostructure, elemental distribution, phase composition and phase distribution of these coatings (and the effects of post-coat annealing on these features) were investigated.

Analyses via conventional transmission electron microscopy (TEM), high resolution (HR)TEM and/or scanning (S)TEM were then carried out. For each selected sample, either plan-view or cross-section (or both) thin-foil TEM samples was made. The selection and type (plan-view or cross-section) of TEM thin-foil samples to be prepared were based on the results of previous studies [34] (i.e. SE/BSE imaging, EDX point analyses and mapping, together with XRD analysis). Conventional TEM was carried using a Philips EM420 and a FEI Tecnai T20, operated at 120KeV and 200KeV, respectively; these instruments were used to obtain bright field (BF) and dark field (DF) images, with corresponding selected-area electron diffraction (SAED) patterns. HRTEM imaging, STEM bright field and high angle annular dark field (HAADF) imaging, together with energy-filtered (EF)TEM elemental mapping were carried out using a JEOL 2010F S/TEM equipped with a Schottky field emission gun (operated at 200KeV), a Gatan Imaging Filter (GIF) 794 spectrometer, and Gatan Digiscan STEM BF and HAADF detectors. All TEM samples were prepared using an FEI Quanta 200 3D scanning electron microscope equipped with Ga^+ Focused Ion Beam (FIB).

In order to simplify the following discussion, each sample (or the deposited coating thereon) from the 3×3 matrix will be simply described using the names shown in Fig. 1(a) (T, M, B; L, C, R stand for Top, Middle and Bottom; Left, Centre and Right, respectively; e.g. ‘TL’ indicates the top-left sample). As-deposited coatings without annealing will be described as ‘XY-AD’ (where ‘X’ = T, M or B; ‘Y’ = L, C or R; ‘AD’ means as-deposited). Coatings annealed at 300 ℃ and 500 ℃, will be described as ‘XY-300’ and ‘XY-500’, respectively. ‘Column’ is used to describe a set of 3 samples distributed in the vertical direction; similarly, ‘row’ is used to describe a set of 3 samples distributed in horizontally. By analogy, several descriptive examples are listed below: XL indicates the 3-sample set of TL, ML and BL (in all three post-deposition annealing conditions); TY-500 indicates the 3-sample set of TL-500, TC-500 and TR-500; TL-Cr indicates chromium (concentration) in the top-left sample, etc.

3. Results and discussion

3.1. Coating thickness and elemental compositions

3.1.1. Coating thicknesses

The as-deposited coating thicknesses corresponding to each sample position are listed in Table 1, and a detailed discussion corresponding to coating thicknesses and deposition rates obtained in the described CFUBMS system configuration can be found elsewhere [34].

3.1.2. Elemental composition

Table 2 lists the elemental concentrations of the 4 constituents – Cr, Cu, Ag and N – in each as-deposited coating, in atomic percentage.

From Table 2, it can be seen that from top to bottom, Cr concentration decreases while Cu and Ag concentrations increase, within the same column. In addition, from left to right, Cu concentration decreases while Ag concentration increases, within the same row. The trends of elemental composition variation agree well with the intentionally arranged substrate configuration, in order to obtain specific substrate-target distances for each sample (see Fig. 1), and hence regularly and systematically varying compositions.

3.2. X-ray diffraction results and discussion

3.2.1. Overall information

The XRD patterns of as-deposited and annealed coatings are plotted in Fig. 2. In order to deal with the “overlapping” problem of Cr, Cr_2N, Cu, Ag and substrate austenitic peaks (AISI316 stainless steel) at 2θ ranges of 37° to 39° and 42° to 45°, a break (46° to 46.5°) at the 2-Theta axis was introduced and the range 35° to 45° (will be called “overlapping zone” or OLZ in the following discussion) was scaled to 75% of the whole 2-Theta axis range (35° - 90°). The OLZ can be revealed thereby, with much more detail (where overlapping peaks would otherwise hardly be distinguished). Moreover, there are significant peak intensity differences among coatings after different post-deposition treatments; therefore, in order to distinguish most peaks in the XRD patterns, different intensity scales were used: the intensity ratios among Figs. 2a to 2c are 1:10:20, respectively. It should also be mentioned that the atom radii of the 4 constituents, Cr, Cu, Ag and N, are 1.66Å, 1.45 Å, 1.65 Å and 0.56 Å, respectively [35].

3.2.2. The as-deposited coatings

Fig. 2a shows the XRD patterns of the as-deposited coatings. All as-deposited coatings only show one primary reflection (except the TR-AD pattern, which shows two reflections with similar intensities, Cr(110) and Cr(200), respectively). Considering their much lower-intensity and broader peaks (comparing with Figs. 2b and 2c, and recalling remember the scale ratios stated above), and also the intrinsic immiscibility between each pair of the three transition-metal constituents (Cr-Cu, Cr-Cu and Ag-Ag) [36-39], several preliminary conclusions can be drawn. Firstly, each as-deposited coating is composed of one primary solid solution (including TR-AD, which has a bcc-Cr matrix); secondly, the solid solutions are all supersaturated, which inevitably causes extreme lattice distortion; thirdly, these solid solutions might exist as ultrafine nanocrystallites, which (although not easy to confirm using XRD alone), is usually the case for PVD coatings deposited at low substrate temperatures. Coatings with low Cu+Ag concentrations, e.g. TL, TC and TR, exhibited a broad reflection of Cr(110), shifted to lower angles of 2θ, indicating an expanded lattice parameter. No other reflections were found (except a Cr(200) reflection for TR), indicating that TL-AD, TC-AD and TR-AD are each composed of a bcc α-Cr-matrix solid solution, with strong preferred orientation (will be discussed further in the TEM and STEM investigation). As the Cu+Ag concentration increases, the 'matrix' of the solid solution changes.

3.2.3. The coatings annealed at 300 ℃

As shown in Fig 2b, after annealing at 300 ^{o}C for 2 hours, lattice reflections become sharper and much higher in intensity, compared to those of the as-deposited coatings (note that the intensity scale of Fig. 2c is 10 times that of 2a). Overall, as Cu and/or Ag concentration increases in the coating, stronger reflections of their crystalline phases emerge. Moreover, these Cu and Ag reflections appear close to their theoretical 2θ values, indicating the relaxation of lattice distortion compared to their as-deposited analogues and strong rejection to other elements dissolved in substitutional/interstitial solid solution. Furthermore, for those coatings that show clear fcc-Cu and/or Ag reflections, clear bcc-Cr reflections also arise, confirming the rejection (and separate precipitation) of Cr from the fcc-Cu or Ag matrix. By combining the fact that no Cr nitride reflections (from Cr_2N or CrN) are found, the following conclusions can be drawn: (1) the metastable fcc-matrix solid solutions formed by PVD on substrates without external heating are extremely thermodynamically unstable, and under annealing, even at relatively low temperatures (e.g. 300^{o}C), will readily unmix and transform into more stable phases by the precipitation of substitutional elements (e.g. MR-AD primarily composed of fcc (Ag, Cr), while MR-300 composed of fcc Ag and precipitated bcc Cr); (2) bcc-Cr PVD solid solutions deposited in-situ are relatively stable, and retain their crystallographic structure under low temperature annealing; this is clearly also partially due however to the relatively low Cu+Ag concentrations; (3) N probably exists in the Cr-matrix as an interstitial solid solution.

3.2.4. The coatings annealed at 500 ℃

After annealing at 500 ℃ for 2 hours, as shown in Fig 9c, all coatings exhibit clear Cr_2N(111) and Cr(110) reflections, covering a surprisingly large range of N/(Cr+N) ratios from 0.11 to 0.55 (see Table 2.). No CrN reflections can be found, even for BR-500, which has rather high a N/(Cr+N) ratio of 0.55. It is interesting to compare the phase transformation of coatings TR and MC between the two annealed states. It is expected that TR-500 and MC-500 exhibit sharper and slightly higher Ag(111) reflections than TR-300 and MC-300, respectively, resulting from the temperature-induced thermodynamics on the precipitation process of Ag However, MC-500 exhibits a sharper and much higher reflection of Ag(111) than TR-500. This behaviour contradicts the actual Ag atomic concentrations of TR (12.4 at.%) and MC(4.1 at.%), whereas it does relate to some extent with the Cu concentration (5.1 at.% and 19.3 at.% for TR and MC, respectively) and correlate more closely to the (Cu+Ag) combined contents. In other words, although decreasing in concentration, Ag shows much enhanced precipitation with increasing Cu concentration in PVD Cr-N based coatings, which will be further verified by the following TEM and STEM analyses.

3.3. TEM and STEM results and discussion

3.3.1. Coating selection principles for TEM and STEM investigation

Sample positions TR, MC and MR were selected for detailed TEM analysis, to further investigate the phase compositions and annealing-induced phase transformations of CrCuAgN coatings. The selection of these representative samples was based on the findings of our previous study [34], based on principles of (a) changes in as-deposited primary matrix (i.e. bcc-Cr matrix or fcc-Ag matrix); (b) reasonably high Cu+Ag concentration (greater than 15 at.%, but no more than 35 at.%); (c) a sufficiently broad variation in Ag/Cu ratios (i.e. from less than 0.5 to more than 5). In detail:

TR – TR-AD exhibits a bcc-Cr matrix, a Cu+Ag concentration of 17.5 at.%, and relatively high in Ag concentration. Four TEM samples were prepared, which were TR-AD cross-section, TR-AD plan-view, TR-500 cross-section and TR-500 plan-view, respectively.

MC – MC-AD exhibits a bcc-Cr matrix, a Cu+Ag concentration of 23.4 at.%, and a low Ag/Cu ratio. One TEM sample was prepared, which was MC-500 cross-section;

MR – MR-AD exhibits an fcc-Ag matrix, a Cu+Ag concentration of 34 at.%, and a high Ag/Cu ratio. Four TEM samples were prepared, which were MR-AD cross-section, MR-AD plan-view, MR-500 cross-section and MR-500 plan-view, respectively.

The selected coatings and corresponding annealed conditions for TEM and STEM analyses were also shown in Table 3.

3.3.2. TEM and STEM results and discussion on selected samples

3.3.2.1. TR-AD

The bright field (BF) and dark field (DF) images of TR-AD cross-section and TR-AD plan-view are shown in Figs. 3 and 4, respectively. BF and DF images were taken from the same area, at both low and high magnifications, with corresponding selected area electron diffraction (SAED) patterns also shown in the centre of each figure.

For the TR-AD cross-section, a clear columnar structure can be seen from Figs. 3a and c. From Fig. 3d, it can also be seen that the grain sizes of TR-AD are less than 5 nm, even sub-nanometre within the current cross-section view. . The SAED pattern in the centre (Fig.2e), which is composed of discontinuous diffraction ring segments rather than periodically distributed spots, further confirms the existence of ultrafine nanocrystallites, with a bcc-Cr structure. Fig. 3e also indicates that the nanocrystallites exhibit a strong preferred orientation of <110> along the film growth direction. Obviously, another view from a different angle is required to confirm the 3D shapes of these grains, therefore a plan-view sample, namely plan-view TR-AD, was also prepared for further investigation.

For the TR-AD plan-view, cross-sections of the columnar coating growth morphology visible in Fig.2 can be seen from Fig. 4, with column diameters apparently in a range between 100 and 300 nm. An individual column was chosen for investigation at higher magnification, as seen in Figs. 4b and 4d, which reveal that grain sizes under plan view are also less than 5 nm. By combining the cross-section and plan-view investigations of TR-AD, it can now be confirmed that TR-AD is composed of equiaxial nanocrystallites. The SAED pattern (Fig. 4e) further confirms that the nanocrystallites are ultrafine bcc-Cr, in accordance with Fig. 3e. Fig. 4e also indicates no existence of lateral preferred orientation.

Only bcc Cr diffraction rings were found from both the cross-section and plan-view SAED patterns, indicating strongly that the other constituents, Cu, Ag and N, exist in solid solution in the bcc α-Cr-matrix. Therefore, significant lattice distortion would be expected in the Cr matrix, and this can be seen in Fig. 5a, which shows a high resolution TEM image taken from the Cr[100] zone axis, with its Inverse Fast Fourier Transform (IFFT) image shown in

Fig. 5b. A large number of stacking faults (e.g. “disappearing” atomic planes, indicated by red arrows) together with a significantly distorted lattice (e.g. distorted atomic planes indicated by the red, curved lines), can be clearly seen from Fig. 5b.

3.3.2.2. TR-500

For the sample TR-500 cross-section, low magnification BF and high-angle annular dark field (HAADF) images at low magnification are shown in Fig. 6. It can be seen that the surface of TR is quite rough, and the columnar structure from the as-deposited state partially remained after annealing at 500 ℃. Moreover, the nanocrystallites in the coating vary significantly in their range of sizes, and distributed unevenly.

HAADF images, with corresponding EDX elemental mapping acquired at medium and high magnification are shown in Fig. 7. It can be seen that a large number of Cu and Ag nanocrystallites, in sizes of 20 nm to 200 nm, precipitated from the bcc-Cr matrix during annealing at 500 ℃. A colourised image, constructed by combining 5 different DF images taken from TR-500 plan-view is shown in Fig. 8, with the corresponding SAED pattern and BF image for better illustration. Fig. 8 clearly exhibits the plan-view morphologies and size distributions of the mixture of Cr, Cr_2N and Ag nanocrystallites. However, only a fraction of the nanocrystallites seen in the BF image of Fig. 8b are “inserted” into Fig. 8c (note the numbers of spots inside and outside the coloured circles of Fig. 7a).

Mulligan et al. [29] proposed that the Ag transport in CrN-Ag coatings is detachment-limited rather than diffusion-limited. Their analysis was based on the Gibbs-Thomson effect [40] and related to the particle coarsening (Ostwald ripening) [41], and explained the behaviour of Ag transport during annealing in PVD CrN-Ag coatings. The chemical potential change $\Delta\mu$ with the size of a spherical particle can be calculated by [14, 40]:

$$\Delta\mu = \Delta P \cdot \mathrm{V_m} = \frac{2}{\ }$$

where ΔP is the additional external pressure imposed on the particle due to its surface energy, V_m, γ and r are the molar volume, surface energy and radius of the spherical particle, respectively. Therefore, a smaller particle (larger curvature) possesses higher chemical potential, hence higher driving force for it to dissolve, resulting in a higher detachment rate of it compared to larger particles under identical conditions. For CrCuAgN coatings in this study, similar behaviours have been found for both Ag and Cu transportation. As can be seen from Fig. 7b, larger Cu and Ag particles are found in the near-surface area, and relatively smaller Cu and Ag nanocrystallites are distributed in the whole coating cross section, with no obvious diffusion gradient layer found either between the precipitates and the solid-solution matrix, or across the CrCuAgN coating (i.e. from the substrate-coating interface to the coating surface). This fact indicates sufficiently fast (if not fully completed yet) precipitation of Ag and Cu from the solid-solution matrix during vacuum annealing at 500 ℃. In other words, it means that the precipitation process of both Ag and Cu mainly depends on the varying detachment rates of different-sized particles, and is not limited by the diffusion speed which is sufficiently high. Fig. 9 shows a large Ag nanocrystallite (red) merging with a smaller Ag nanocrystallite (green), from TR-500 plan-view. Note that their boundary is extremely flat, indicating that the chemical potential (proportional to the radius of curvature) tends to remain as low as possible during the merging.

3.3.2.3. MC-500

For sample MC-500 cross-section, the HAADF images and corresponding colourised RGB EDX mapping images at relatively low and high magnifications are shown in Fig. 10. As can be seen from Figs. 10a and 10c, the nanocrystallites are equiaxial. Moreover, Figs. 10b and d demonstrate that Cu and Ag precipitates are of a similar size and are distributed homogeneously throughout the coating thickness, which is a more desired nanostructure than that shown for TR-500 in Fig. 6. After the original Cu and Ag precipitation across the coating, smaller precipitates (with higher chemical potentials), which have higher detachment rates, merge with larger ones, which will be constrained inside the coating. Finally, due to the reduced mechanical constraint of the precipitates in the surface region, they aggregate and grow larger in size, as discussed in section 3.3.2 and shown in Figs. 7 and 8. Larger Cu aggregates near the coating surface can be seen from Figs. 10b and d. The square area selected in Fig. 10d was chosen to obtain a clearer colourised and stitched elemental map using the 3-window method in energy filtered (EF)TEM, which is shown in Fig. 11. It can clearly be seen from Fig. 11 that Cu grains (in green) near the surface are larger than those further from surface. Large Ag nanocrystallites (in blue) are found next to Cu grains; taking into account their atomic concentrations in MC (Cu: 19.3 at.%; Ag: 4.1 at.%) and the much larger grain size of Cu than Ag, it may be deduced therefore that Cu exhibits higher detachment rate than Ag, hence a positive effect on Ag transport to the coating surface.

A colourised image constructed by combining 10 different DF images taken from MC-500 cross-section is shown in Fig. 12 (similar to Fig. 8). It clearly exhibits the different cross-sectional morphologies, sizes and crystallographic orientations of the Cr, Cr_2N, Cu and Ag nanocrystallites. Similar to TR-500 in Fig. 8, only a portion of the nanocrystallites in the view of Fig. 12b are “inserted” into Fig. 12c (note the number of spots inside and outside the colour circles in Fig. 12a).

3.3.2.4. MR-AD

For sample MR-AD in cross-section, its BF and DF images from conventional TEM analysis are shown in Fig. 13. BF and DF images were taken from the same area, at both low and high magnifications, with the corresponding selected area electron diffraction (SAED) patterns also shown in the centre of the figure. The SAED pattern (Fig. 13e) confirms that MR-AD has a fcc-Ag based matrix, and strong preferential orientation of <111. This fcc-Ag-matrix coating also exhibited a clear columnar growth structure, with the columns containing nanocrystallites less than 5 nm in width (see Fig. 13d).

For sample MR-AD in plan-view, an elemental map acquired by EFTEM using the 3-window method is shown in Fig. 14. Fluctuations in Cr, Ag and Cu concentrations over distances less than 5 nm in width can be seen, indicating that the Ag-based matrix solid solution is not homogeneous in elemental distribution. Note that the chemical composition of MR is Cr: 37.2 at.%, Cu: 4.5 at.%, Ag: 29.5 at.% and N: 28.7 at.%, respectively, resulting in the RGB EFTEM image (Fig. 14) was dominated by Cr (red) and Ag (blue), with the low-concentration Cu (blue) being barely visible. The pre-existence of concentration fluctuations could be beneficial in the precipitation of Cu and/or Ag as solid lubricants under medium-high temperature (e.g. 500 ℃) service.

3.3.2.5. MR-500

For sample MR-500 cross-section, HAADF images and corresponding RGB EDX elemental mapping at low, medium and high magnification are shown in Fig. 15. The cross section sample was taken by cutting through 2 large precipitates (similar to those shown in Fig. 9).

Fig. 15a shows that after annealing at 500 ℃, the columnar structure of MR-AD (Fig. 13) disappeared and the entire coating is filled with nanocrystallites. Most nanocrystallites are equiaxed, however, a portion of them are elongated along the original columnar direction, as indicated using green ellipses. Fig. 15b reveals that Cr and Ag distribute homogeneously inside the coating; however, Cu precipitates are obviously aggregated, both inside the coating and on the coating surface. Moreover, despite the relatively low concentration of Cu in MR (Ag: 29.5 at.%; Cu: 4.5 at.%), Cu aggregates are larger than Ag aggregates (see the large green Cu aggregates in Fig. 15b) , indicating much higher dissolving rate of small Cu precipitates than Ag. In other words, Cu precipitates possess much higher detachment rate than Ag precipitates, in agreement with the conclusion drawn in section 3.4. Furthermore, most of the large aggregates on the coating surfaces are found to be fused Cu and Ag, with clear boundaries (see Fig. 15b). Therefore, a further conclusion can be drawn: when annealed at a moderately high temperature (500 ℃), Cu in solid solution would quickly precipitate and aggregate into larger fused clusters, leaving voids in the original solid solution which may then be conducive to subsequent Ag precipitation, both inside the coating and on the coating surface. In other words, by proper design and processing, CrCuAgN coatings with appropriate elemental compositions and solid-solution matrix can be obtained, in which the precipitation rate of Ag can be partially controlled by the concentration of Cu (which need not necessarily be high - since, in MR, 4.5 at.% Cu seems to be more than sufficient), resulting in control of the supplementation rate of the desired active ingredients (in this case, Ag).

Figs. 15c to 15f exhibit the two squared areas indicated in Fig. 15a at medium and high magnifications. It can be seen (especially from Fig. 15f) that spherical Cr-containing (Cr or Cr_2N) nanocrystallites precipitate from the Ag matrix. No particular shape was found for Cu nanocrystallites inside the coating, probably because they aggregate quite quickly by taking any available voids formed by other precipitates. The large Cu aggregates on the coating surface are polygonal (Fig. 15b).

The solid lubricating properties of similar CrCuAgN coatings to those reported here have been exhibited in an earlier publication [17].

Conclusions

CrCuAgN coatings were produced by CFUMBS on mirror-finish AISI316L stainless steel coupons without external heating, in a 3×3 matrix configuration. Then the effects of post-coat annealing on the nanostructure of as-deposited coatings were studied. The following conclusions can be drawn:

i. Each as-deposited coating is composed of one primary solid solution. Moreover, the solid solutions are all supersaturated, exhibiting a strong texture. Furthermore, different elemental compositions of CrCuAgN coatings could result in different solid-solution matrices. In this study, bcc-Cr-matrix, fcc-Cu-matrix and fcc-Ag-matrix solid solutions were found, depending on the major elemental constituent. No fcc-CrN was found in any coatings, even in those possessing a N/(Cr+N) ratio as high as 0.55 (i.e. N/Cr ratio over 1.2).

ii. The as-deposited coatings exist as ultra-fine nanocrystallites and possess extremely distorted lattices, as well as a high density of stacking faults.

iii. Both Cu and Ag aggregated on coating surfaces after annealing at 500 °C. During annealing, Cu precipitates exhibited higher growth rates than Ag, hence Cu grains being larger than Ag grains, even for coatings possessing a significantly higher concentration of Ag than Cu.

iv. The aggregation of both Cu and Ag are detachment-limited, rather than diffusion-limited.

v. Fluctuations in Cr, Ag and Cu distribution in a scale of less than 5 nm dimension was found, which could be beneficial in the precipitation of Cu and/or Ag as solid lubricants under moderately high temperature (e.g. 500 ℃) service.

vi. The co-existence of Cu with Ag in a PVD metallic coating was found to be beneficial to enhanced Ag transport onto the coating surfaces, resulting not from the anticipated “intergranular network channels” of Cu, but from the much higher detachment rate of Cu than Ag, which can leave pathways for Ag to migrate after Cu depletion. Nevertheless, the potential for CrCuAgN coatings with a desired nanostructure to be obtained via appropriate coating/process design is clear, and specific nanostructures that correspond to a controlled precipitation rate of Ag (depending on coating composition and annealing temperature) can be created for different practical applications, by varying the concentration of Cu in the Cr-Cu-Ag-N system, and the option of optimised annealing procedure as well.

References

[1] P. Basnyat, B. Luster, Z. Kertzman, S. Stadler, P. Kohli, S. Aouadi, J. Xu, S. Mishra, O. Eryilmaz, A. Erdemir, Mechanical and tribological properties of CrAlN-Ag self-lubricating films, Surface and Coatings Technology 202(4) (2007) 1011-1016.

[2] V. Ezirmik, E. Senel, K. Kazmanli, A. Erdemir, M. Ürgen, Effect of copper addition on the temperature dependent reciprocating wear behaviour of CrN coatings, Surface and Coatings Technology 202(4-7) (2007) 866-870.

[3] H.C. Barshilia, N. Selvakumar, B. Deepthi, K. Rajam, A comparative study of reactive direct current magnetron sputtered CrAlN and CrN coatings, Surface and Coatings Technology 201(6) (2006) 2193-2201.

[4] T. Elangovan, P. Kuppusami, R. Thirumurugesan, C. Sudha, E. Mohandas, D. Mangalaraj, A Study on the Influence of Copper Content in CrN/Cu Nanocomposite Thin Films Prepared by Pulsed DC Magnetron Sputtering, Journal of Nanoscience and Nanotechnology 9(9) (2009) 5436-5440.

[5] L. Incerti, A. Rota, S. Valeri, A. Miguel, J. García, R. Rodríguez, J. Osés, Nanostructured self-lubricating CrN-Ag films deposited by PVD arc discharge and magnetron sputtering, Vacuum 85(12) (2011) 1108-1113.

[6] P. Papi, C. Mulligan, D. Gall, CrN-Ag Nanocomposite Coatings: Control of Lubricant Transport by Diffusion Barriers, Thin solid films (2012) 211-217.

[7] O. Jimenez, M. Audronis, M. Baker, A. Matthews, A. Leyland, Structure and mechanical properties of nitrogen-containing Zr–Cu based thin films deposited by pulsed magnetron sputtering, Journal of Physics D: Applied Physics 41 (2008) 155301.

[8] J.L. Endrino, J.J. Nainaparampil, J.E. Krzanowski, Microstructure and vacuum tribology of TiC–Ag composite coatings deposited by magnetron sputtering-pulsed laser deposition, Surface and Coatings Technology 157(1) (2002) 95-101.

[9] Y. Wang, J. Wang, G. Zhang, L. Wang, P. Yan, Microstructure and tribology of TiC (Ag)/aC: H nanocomposite coatings deposited by unbalanced magnetron sputtering, Surface and Coatings Technology 206(14) (2012) 3299-3308.

[10] A. Voevodin, J. Hu, J. Jones, T. Fitz, J. Zabinski, Growth and structural characterization of yttria-stabilized zirconia–gold nanocomposite films with improved toughness, Thin solid films 401(1) (2001) 187-195.

[11] C. Muratore, A. Voevodin, J. Hu, J. Zabinski, Tribology of adaptive nanocomposite yttria-stabilized zirconia coatings containing silver and molybdenum from 25 to 700 C, Wear 261(7) (2006) 797-805.

[12] C. Muratore, J. Hu, A. Voevodin, Adaptive nanocomposite coatings with a titanium nitride diffusion barrier mask for high-temperature tribological applications, Thin solid films 515(7) (2007) 3638-3643.

[13] K. Kutschej, C. Mitterer, C.P. Mulligan, D. Gall, High ‐ Temperature Tribological Behavior of CrN ‐ Ag Self ‐ lubricating Coatings, Advanced Engineering Materials 8(11) (2006) 1125-1129.

[14] C. Mulligan, T. Blanchet, D. Gall, CrN–Ag nanocomposite coatings: High-temperature tribological response, Wear 269(1) (2010) 125-131.

[15] C. Mulligan, T. Blanchet, D. Gall, CrN–Ag nanocomposite coatings: Tribology at room temperature and during a temperature ramp, Surface and Coatings Technology 204(9) (2010) 1388-1394.

[16] P. Kuppusami, T. Elangovan, S. Murugesan, R. Thirumurugesan, S. Khan, R. George, R. Ramaseshan, R. Divakar, E. Mohandas, D. Mangalaraj, Microstructural, nanomechanical and antibacterial properties of magnetron sputtered nanocomposite thin films of CrN/Cu, Surface Engineering 28(2) (2011) 134-140.

[17] X. Liu, C. Iamvasant, C. Liu, A. Matthews, A. Leyland, CrCuAgN PVD nanocomposite coatings: Effects of annealing on coating morphology and nanostructure, Applied Surface Science 392 (2017) 732-746.

[18] J. Zhao, H. Feng, H. Tang, J. Zheng, Bactericidal and corrosive properties of silver implanted TiN thin films coated on AISI317 stainless steel, Surface and Coatings Technology 201(9) (2007) 5676-5679.

[19] Y.C. Kuo, J.W. Lee, C.J. Wang, Y.J. Chang, The effect of Cu content on the microstructures, mechanical and antibacterial properties of Cr-Cu-N nanocomposite coatings deposited by pulsed DC reactive magnetron sputtering, Surface and Coatings Technology 202(4-7) (2007) 854-860.

[20] P. Kelly, H. Li, K.A. Whitehead, J. Verran, R. Arnell, I. Iordanova, A study of the antimicrobial and tribological properties of TiN/Ag nanocomposite coatings, Surface and Coatings Technology 204(6) (2009) 1137-1140.

[21] K. Dunn, V. Edwards-Jones, The role of Acticoat™ with nanocrystalline silver in the management of burns, Burns 30 (2004) S1-S9.

[22] L. Graziani, E. Quagliarini, M. D'Orazio, The role of roughness and porosity on the self-cleaning and anti-biofouling efficiency of TiO2-Cu and TiO2-Ag nanocoatings applied on fired bricks, Construction and Building Materials 129 (2016) 116-124.

[23] M.C. Cruz, G. Ruano, M. Wolf, D. Hecker, E. Castro Vidaurre, R. Schmittgens, V.B. Rajal, Plasma deposition of silver nanoparticles on ultrafiltration membranes: Antibacterial and anti-biofouling properties, Chemical Engineering Research and Design 94 (2015) 524-537.

[24] Su, Xueju, Development and evaluation of anti-biofouling nano-composite coatings, 8(2) (2013) 1120-1120.

[25] C. Mulligan, T. Blanchet, D. Gall, Control of lubricant transport by a CrN diffusion barrier layer during high-temperature sliding of a CrN–Ag composite coating, Surface and Coatings Technology 205(5) (2010) 1350-1355.

[26] C. Mulligan, D. Gall, CrN–Ag self-lubricating hard coatings, Surface and Coatings Technology 200(5) (2005) 1495-1500.

[27] A. Öztürk, K. Ezirmik, K. Kazmanlı, M. Ürgen, O. Eryılmaz, A. Erdemir, Comparative tribological behaviors of TiN, CrN and MoNCu nanocomposite coatings, Tribology International 41(1) (2008) 49-59.

[28] C. Mulligan, T. Blanchet, D. Gall, CrN–Ag nanocomposite coatings: Effect of growth temperature on the microstructure, Surface and Coatings Technology 203(5) (2008) 584-587.

[29] C. Mulligan, P. Papi, D. Gall, Ag transport in CrN-Ag nanocomposite coatings, Thin solid films (2012) 6774-6779.

[30] H. Holleck, Metastable coatings—prediction of composition and structure, Surface and Coatings Technology 36(1) (1988) 151-159.

[31] M. Baker, P. Kench, M. Joseph, C. Tsotsos, A. Leyland, A. Matthews, The nanostructure and mechanical properties of PVD CrCu (N) coatings, Surface and Coatings Technology 162(2) (2003) 222-227.

[32] J.W. Lee, Y.C. Kuo, Y.C. Chang, Microstructure and mechanical properties of pulsed DC magnetron sputtered nanocomposite Cr–Cu–N thin films, Surface and Coatings Technology 201(7) (2006) 4078-4082.
[33] X. Liu, J. Kavanagh, A. Matthews, A. Leyland, The combined effects of Cu and Ag on the nanostructure and mechanical properties of CrCuAgN PVD coatings, Surface and Coatings Technology 284 (2015) 101-111.
[34] X. Liu, Investigation of magnetron sputtered nitrogen-containing chromium coatings with additions of copper and silver, Department of Materials Science and Enigneering, The University of Sheffield, Sheffield, 2017.
[35] E. Clementi, D. Raimondi, W. Reinhardt, Atomic screening constants from SCF functions. II. Atoms with 37 to 86 electrons, The Journal of chemical physics 47(4) (1967) 1300-1307.
[36] T.B. Massalski, H. Okamoto, P. Subramanian, L. Kacprzak, W.W. Scott, Binary alloy phase diagrams, American Society for Metals Metals Park, OH1986.
[37] J. Sanchez, J. Stark, V. Moruzzi, First-principles calculation of the Ag-Cu phase diagram, Physical Review B 44(11) (1991) 5411-5418.
[38] W.G. Moffatt, The handbook of binary phase diagrams, Genium Pub. Corp.1976.
[39] P.R. Subramanian, Phase diagrams of binary copper alloys, Asm Intl1994.
[40] D.A. Porter, K.E. Easterling, Phase transformation in materials, Chapman & Hall, Boundary Row, London (1992) p. 132.
[41] P.W. Voorhees, Ostwald ripening of two-phase mixtures, Annual Review of Materials Science 22(1) (1992) 197-215.

Table Captions

Table 1. Coating thicknesses of the CrCuAgN coatings (in 3x3 array).

Table 2. Elemental concentrations of the CrCuAgN coatings (in 3x3 array).

Table 3. Selected coatings and corresponding annealed conditions for TEM and STEM analyses.

Table 1. Coating thicknesses of the CrCuAgN coatings (in 3x3 array).

	Coating thickness /µm		
	Left (L)	Centre (C)	Right (R)
Top (T)	3.5	1.8	2.9
Middle (M)	4.4	2.4	4.3
Bottom (B)	4.9	2.7	5.5

Table 2. Elemental concentrations of the CrCuAgN coatings (in 3x3 array).

		Concentration /at. %		
Vertical Position	Elements	Left (L)	Centre (C)	Right (R)
Top (T)	N	9.7	11.6	19.2
	Cr	74.6	79.0	63.3
	Cu	13.8	7.7	5.1
	Ag	1.9	1.7	12.4
	N/(Cr+N)	0.11	0.13	0.23
Middle (M)	N	10.9	16.6	28.7
	Cr	56.1	60.0	37.2
	Cu	30.4	19.3	4.5
	Ag	2.6	4.1	29.5
	N/(Cr+N)	0.16	0.22	0.44
Bottom (B)	N	10.6	20.1	28.9
	Cr	35.6	45.8	23.5
	Cu	50.7	26.5	5.2
	Ag	3.1	7.6	42.5
	N/(Cr+N)	0.23	0.30	0.55

Table 3. Selected coatings and corresponding annealed conditions for TEM and STEM analyses.

Position	Left (L)	Centre (C)	Right (R)
Top (T)	--	--	Cross section, as-deposited Plan view, as-deposited Cross section, 500°C annealed Plan view, 500°C annealed
Middle (M)	--	Cross section, 500°C annealed	--
Bottom (B)	--	--	Cross section, as-deposited Plan view, as-deposited Cross section, 500°C annealed Plan view, 500°C annealed

Figure captions

Fig. 1. Schematic drawing of (a) plan-view of target-substrate geometry in the deposition chamber (and sample matrix designation) and (b) vertical arrangement of Cr-Cr-Cu and Cr-Cr-Ag segmented targets.

Fig. 2. X-ray diffraction patterns of CrCuAgN coatings in different post-coat annealing states: (a).as-deposited; (b) annealing at 300 ℃ for 2 hours; (b) annealing at 500 ℃ for 2 hours. Note: the intensity scales were in ratios of 1:10:20, respectively.

Fig. 3. TR-AD cross-section: (a) BF image at low magnification; (b) BF image at high magnification; (c) DF image at low magnification; (d) DF image at high magnification and (e) SAED pattern, with the small red circle (i.e. a schematic drawing illustrating the size and position of the objective aperture) corresponding to selected part of SAED pattern for dark field imaging of (c) and (d).

Fig. 4. TR-AD plan-view: (a) BF image at low magnification; (b) BF image at high magnification; (c) dark field image at low magnification; (d) DF at high magnification and (e) SAED pattern, with the small red circle (i.e. a schematic drawing illustrating the size and position of the objective aperture) corresponding to selected part of SAED pattern for the dark field imaging of (c) and (d).

Fig. 5. Sample TR-AD cross-section: (a) high resolution TEM image taken from Cr[100] zone axis, with growth direction shown by green arrow; (b) IFFT of image (a), with several stacking faults indicated using yellow dashed arrows, and distorted lattice marked by yellow lines.

Fig. 6. TR-500 cross-section: (a) BF image in STEM mode; (b) HAADF image from the same area as (a).

Fig. 7. TR-500 cross-section: (a) HAADF image at medium magnification; (b) RGB EDX mapping image, with corresponding area shown in (a); (c) HAADF image at high magnification, (d) RGB EDX mapping image, with corresponding area shown in (c). Red, green and blue refers to Cr, Cu and Ag, respectively.

Fig. 8. TR-500 plan-view: (a) SAED pattern, with the colour circles (i.e. schematic drawings illustrating the size and positions of the objective aperture used) corresponding to selected spots for DF imaging, and relevant crystal planes are also indicated; (b) the BF image of the corresponding SAED pattern shown in (a); (c) corresponding DF image of (b), processed by overlaying and colourizing of 5 DF images, with same colours as their corresponding marks in (a).

Fig. 9. A large Ag nanocrystallite merging with a small Ag nanocrystallite, from sample TR-500 plan-view.

Fig. 10. MC-500 cross-section: (a) HAADF image at low magnification; (b) RGB EDX elemental mapping, same area as (a); (c) HAADF image at high magnification; (d) RGB EDX mapping image, same area as (c). Red, green and blue refers to Cr, Cu and Ag, respectively.

Fig. 11. MC-500 cross-section: stitched elemental mapping image, using the EFTEM 3-window elemental mapping method of EFTEM. The area corresponds to the squared area shown in Fig. 10d. Red, green and blue refers to Cr, Cu and Ag, respectively.

Fig. 12. MC-500 cross-section: (a) SAED pattern, with the coloured circles corresponding to spots selected (using objective aperture) spots for DF imaging, and relevant crystal planes are also indicated; (b) the BF image of the corresponding SAED pattern shown in (a); (c) corresponding DF image of (b), processed by overlaying and colourizing of 10 DF images, with same colours as their corresponding marks in (a).

Fig. 13. MR-AD cross-section: (a) BF image at low magnification; (b) BF image at high magnification; (c) DF image at low magnification; (d) DF image at high magnification and (e) SAED pattern, with the small red circle corresponding to selected part of SAED pattern for the DF imaging of (c) and (d).

Fig. 14. MR-AD plan-view, elemental mapping image, using the EFTEM 3-window elemental mapping. Red, green and blue refers to Cr, Cu and Ag, respectively. Note that Cr and Ag possess much higher concentration than Cu, resulting in the red-blue (i.e. Cr-Ag) dominated image.

Fig. 15. MR-500 cross-section: (a) HAADF image at low magnification; (b) RGB EDX mapping image, same area as (a). Red, green and blue refers to Cr, Cu and Ag, respectively. Continued.

Fig. 15 (continued). MR-500 cross-section: (c) HAADF image at medium magnification, (d) RGB EDX mapping image, same area as (c); (e) HAADF image at high magnification, (f) RGB EDX mapping image, same area as (e). Red, green and blue refers to Cr, Cu and Ag, respectively.

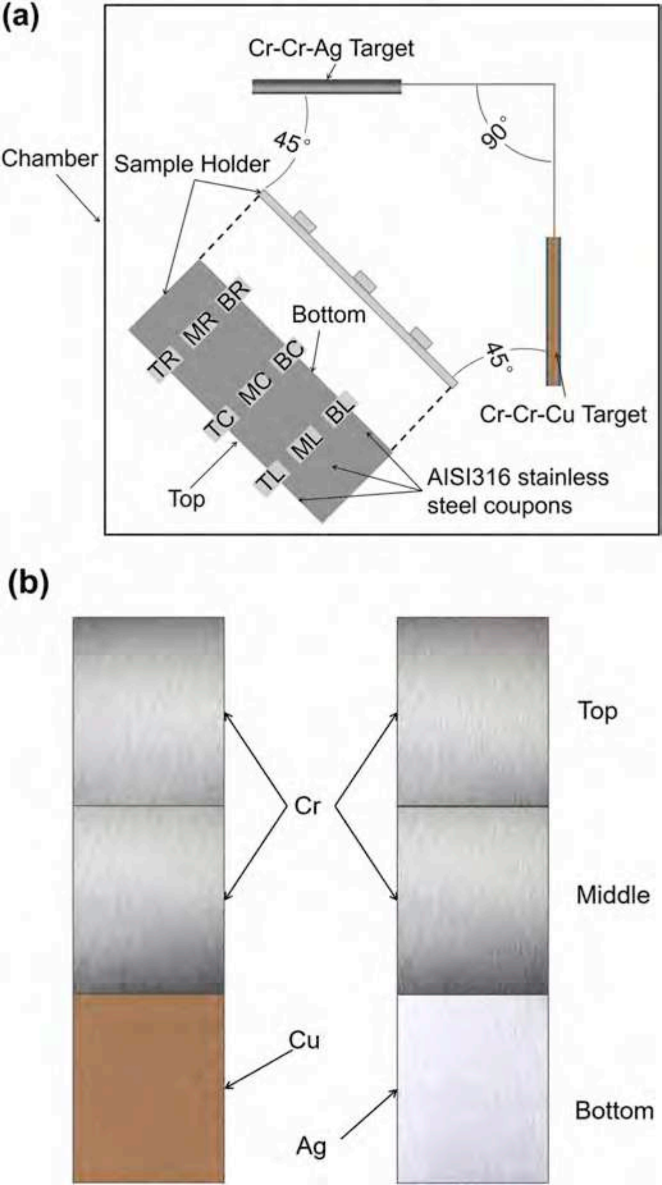
(a)
Cr-Cr-Ag Target
45°
90°
Chamber
Sample Holder
BR
MR
TR
Bottom
BC
MC
TC
BL
ML
TL
45°
Cr-Cr-Cu Target
Top
AISI316 stainless steel coupons
(b)
Top
Cr
Middle
Cu
Bottom
Ag

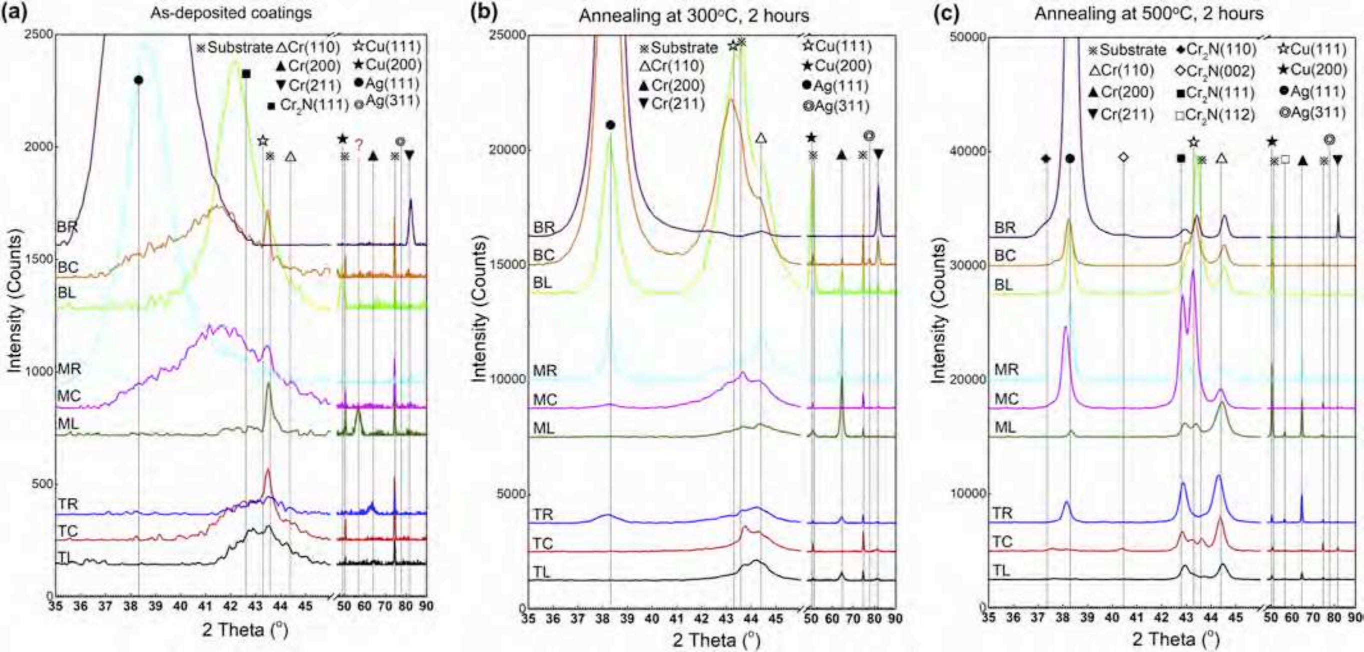
(a)
As-deposited coatings
※Substrate △Cr(110) ☆Cu(111)
▲Cr(200) ★Cu(200)
▼Cr(211) ●Ag(111)
■Cr$_2$N(111) ◎Ag(311)
?
BR
BC
BL
MR
MC
ML
TR
TC
TL
Intensity (Counts)
0
500
1000
1500
2000
2500
35 36 37 38 39 40 41 42 43 44 45 50 60 70 80 90
2 Theta (°)
(b)
Annealing at 300°C, 2 hours
※Substrate
△Cr(110)
▲Cr(200)
▼Cr(211)
☆Cu(111)
★Cu(200)
●Ag(111)
◎Ag(311)
BR
BC
BL
MR
MC
ML
TR
TC
TL
Intensity (Counts)
0
5000
10000
15000
20000
25000
35 36 37 38 39 40 41 42 43 44 45 50 60 70 80 90
2 Theta (°)
(c)
Annealing at 500°C, 2 hours
※Substrate
△Cr(110)
▲Cr(200)
▼Cr(211)
◆Cr$_2$N(110)
◇Cr$_2$N(002)
■Cr$_2$N(111)
□Cr$_2$N(112)
☆Cu(111)
★Cu(200)
●Ag(111)
◎Ag(311)
BR
BC
BL
MR
MC
ML
TR
TC
TL
Intensity (Counts)
0
10000
20000
30000
40000
50000
35 36 37 38 39 40 41 42 43 44 45 50 60 70 80 90
2 Theta (°)

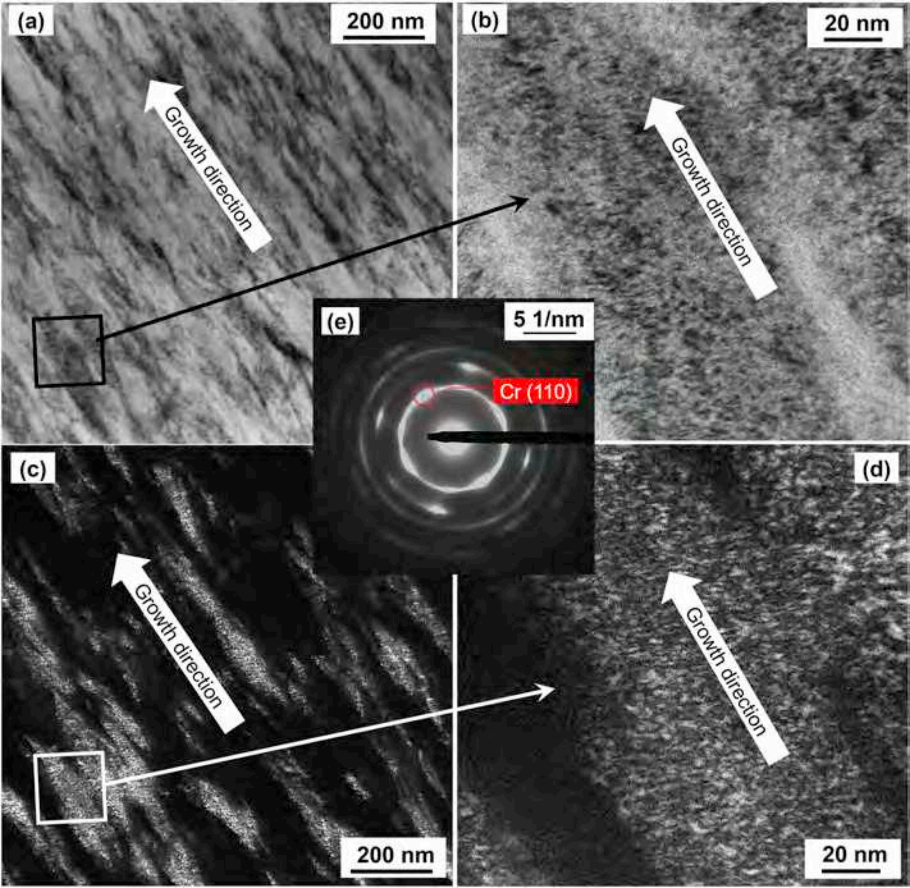
(a)
200 nm
Growth direction
(b)
20 nm
Growth direction
(e)
5 1/nm
Cr (110)
(c)
Growth direction
200 nm
(d)
Growth direction
20 nm

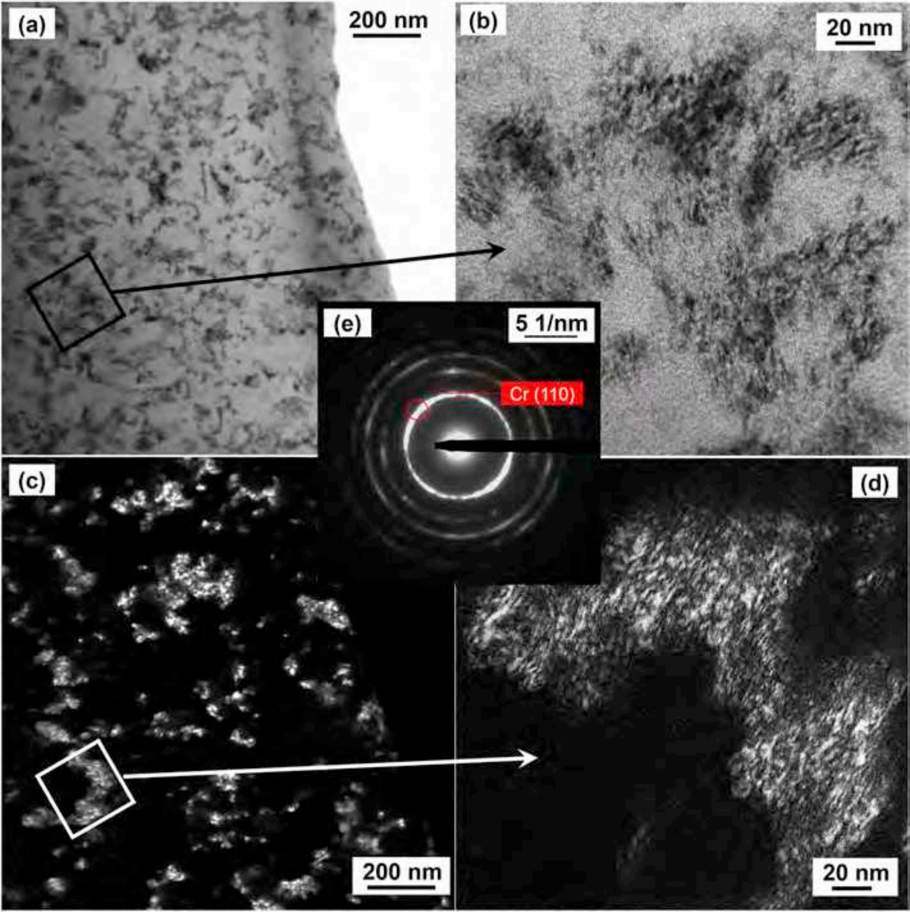
(a)
200 nm
(b)
20 nm
(e)
5 1/nm
Cr (110)
(c)
200 nm
(d)
20 nm

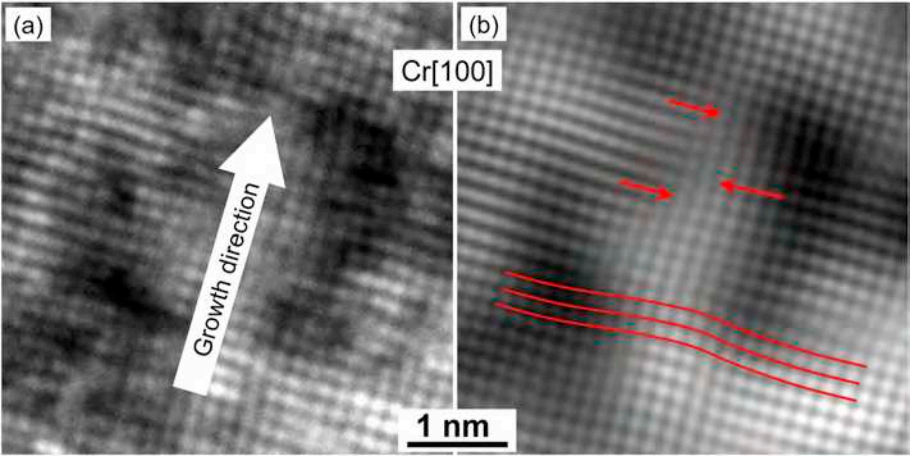
(a)
(b)
Cr[100]
Growth direction
1 nm

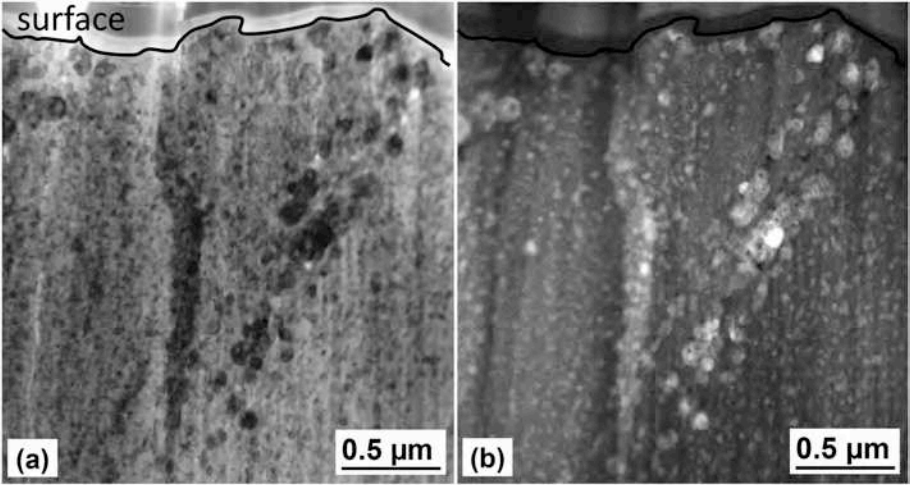
surface
(a)
0.5 µm
(b)
0.5 µm

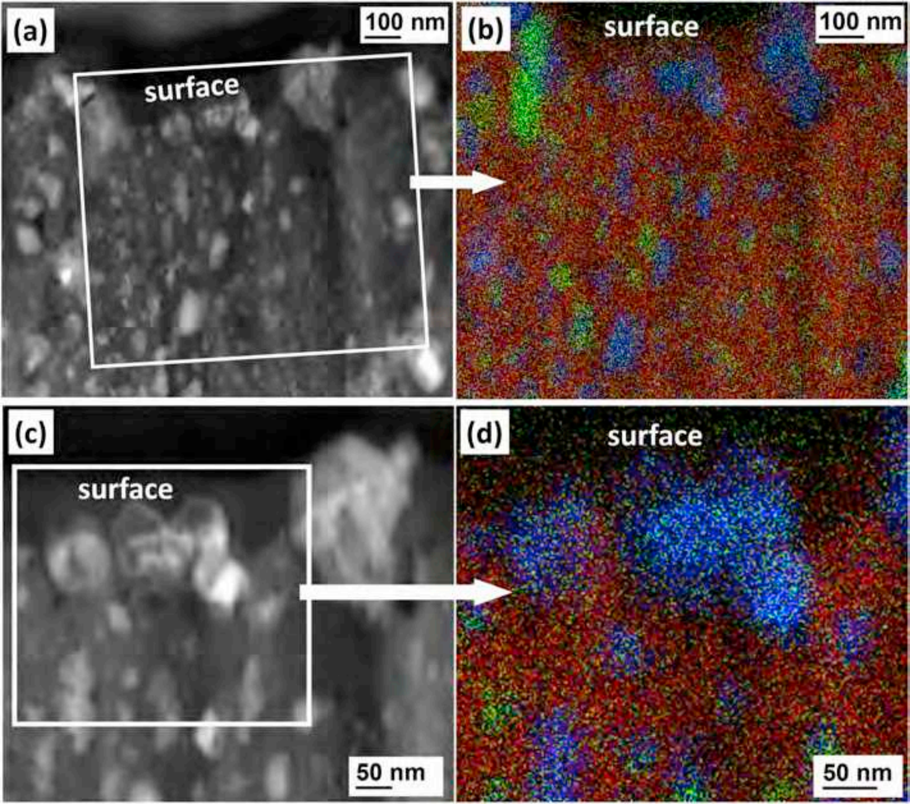
(a)
100 nm
surface
(b)
surface
100 nm
(c)
surface
50 nm
(d)
surface
50 nm

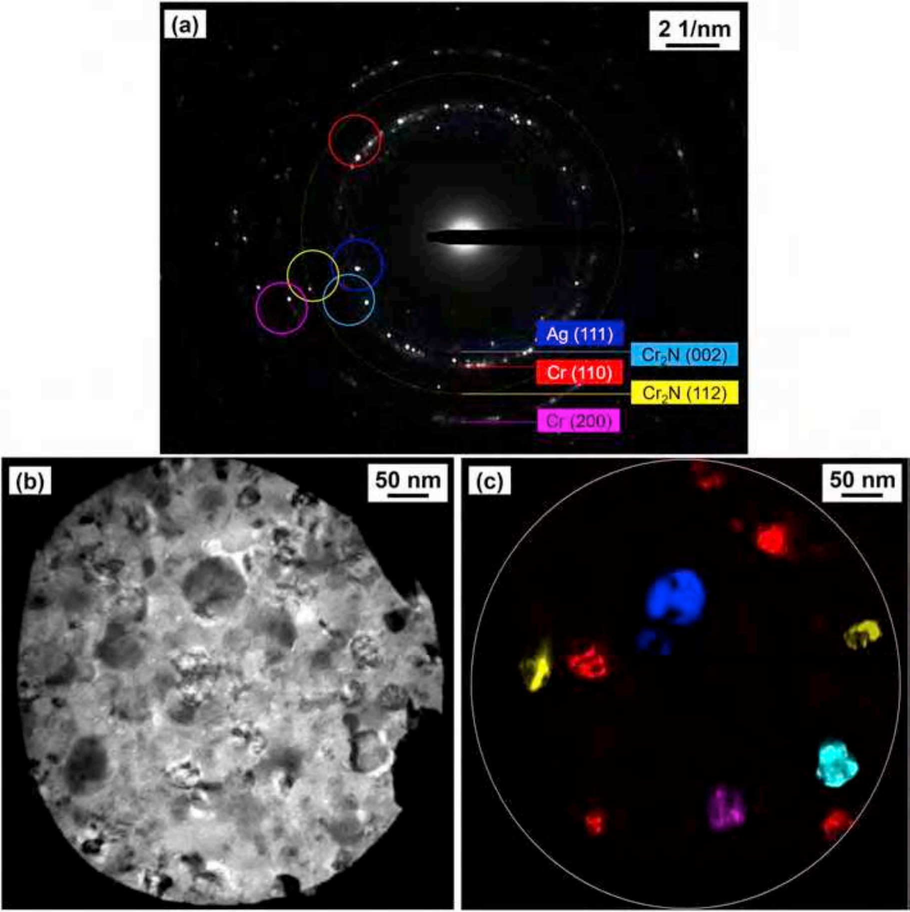
(a)
2 1/nm
Ag (111)
Cr$_2$N (002)
Cr (110)
Cr$_2$N (112)
Cr (200)
(b)
50 nm
(c)
50 nm

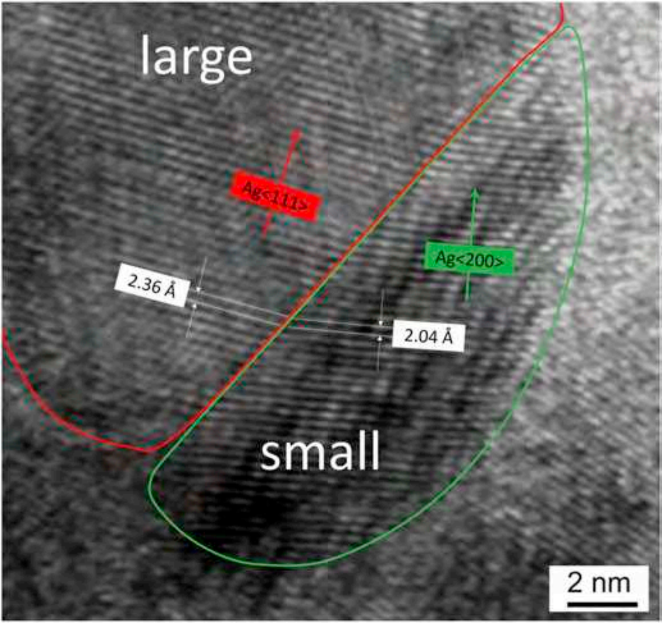
large
Ag<111>
Ag<200>
2.36 Å
2.04 Å
small
2 nm

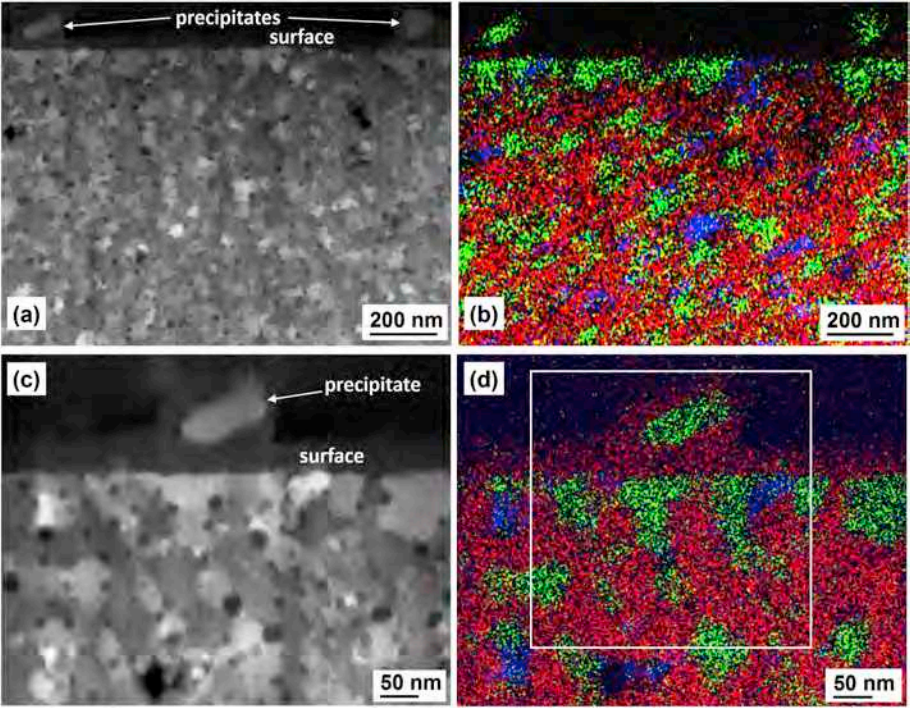
precipitates
surface
(a)
200 nm
(b)
200 nm
(c)
precipitate
surface
50 nm
(d)
50 nm

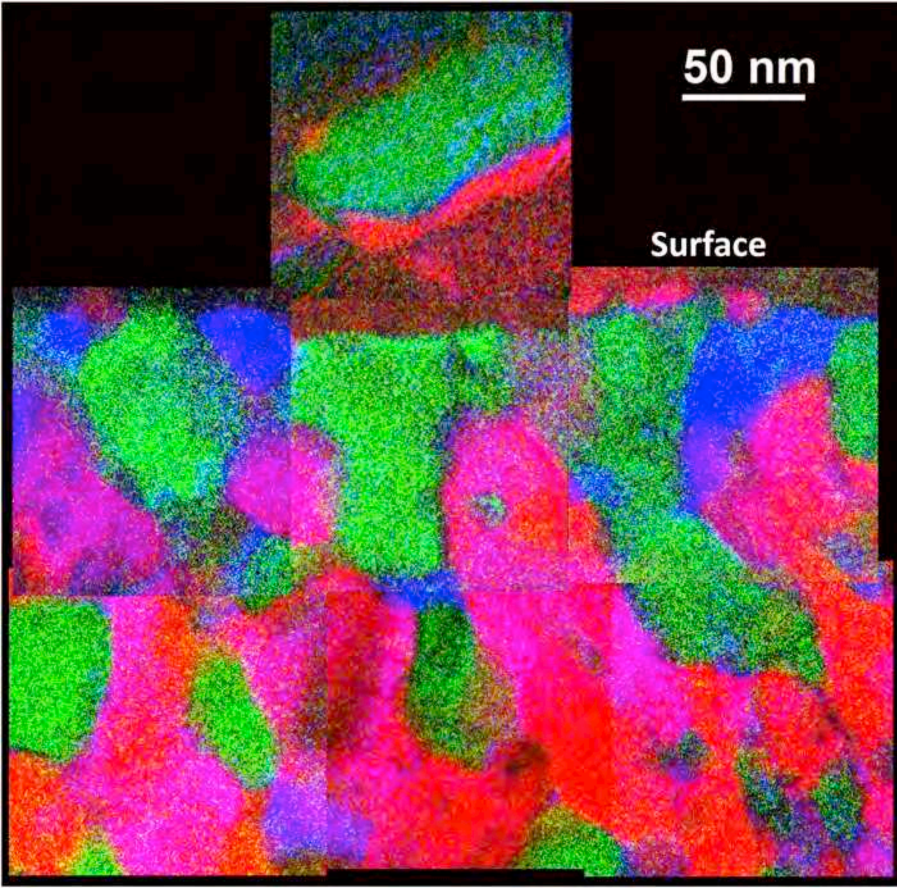
50 nm
Surface

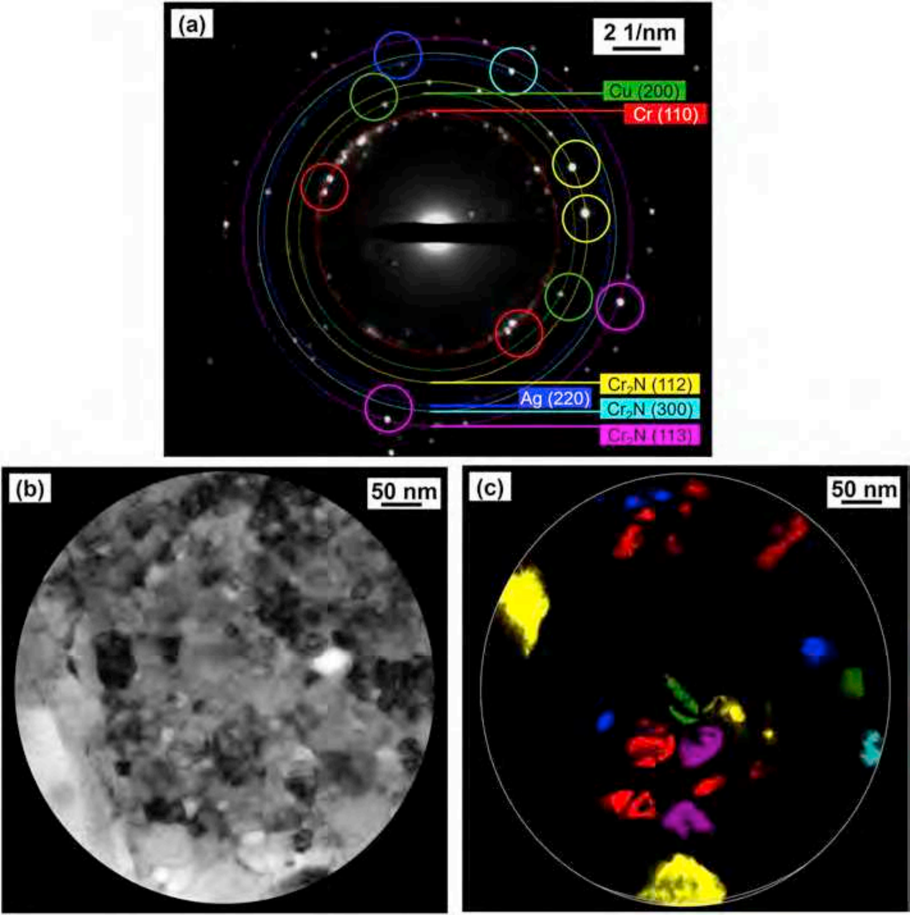
(a)
2 1/nm
Cu (200)
Cr (110)
Cr_2N (112)
Ag (220)
Cr_2N (300)
Cr_2N (113)
(b)
50 nm
(c)
50 nm

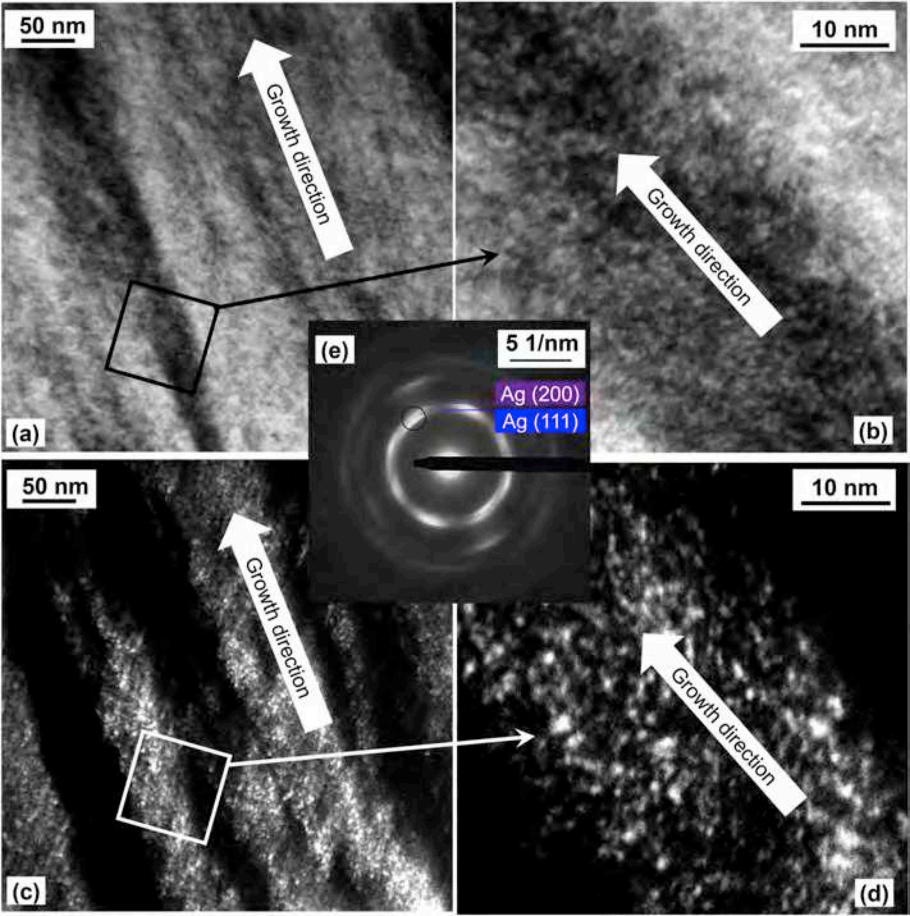
50 nm
Growth direction
10 nm
Growth direction
(a)
(b)
(e)
5 1/nm
Ag (200)
Ag (111)
50 nm
Growth direction
10 nm
Growth direction
(c)
(d)

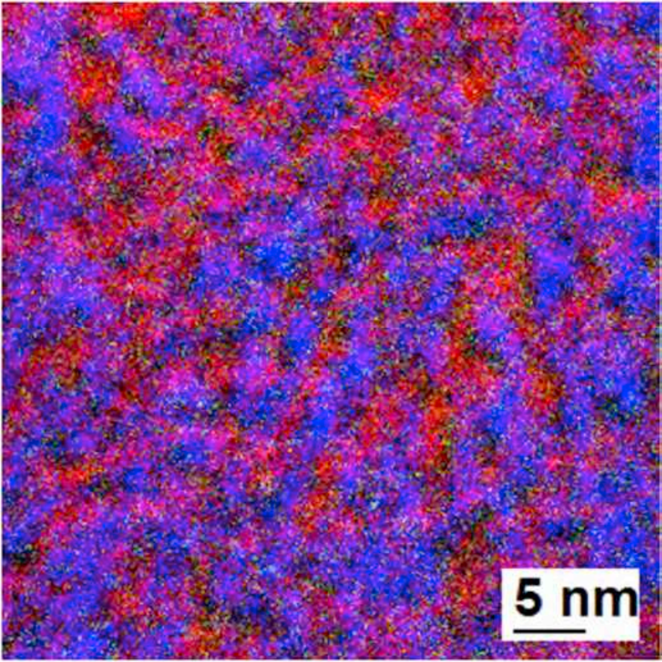
5 nm

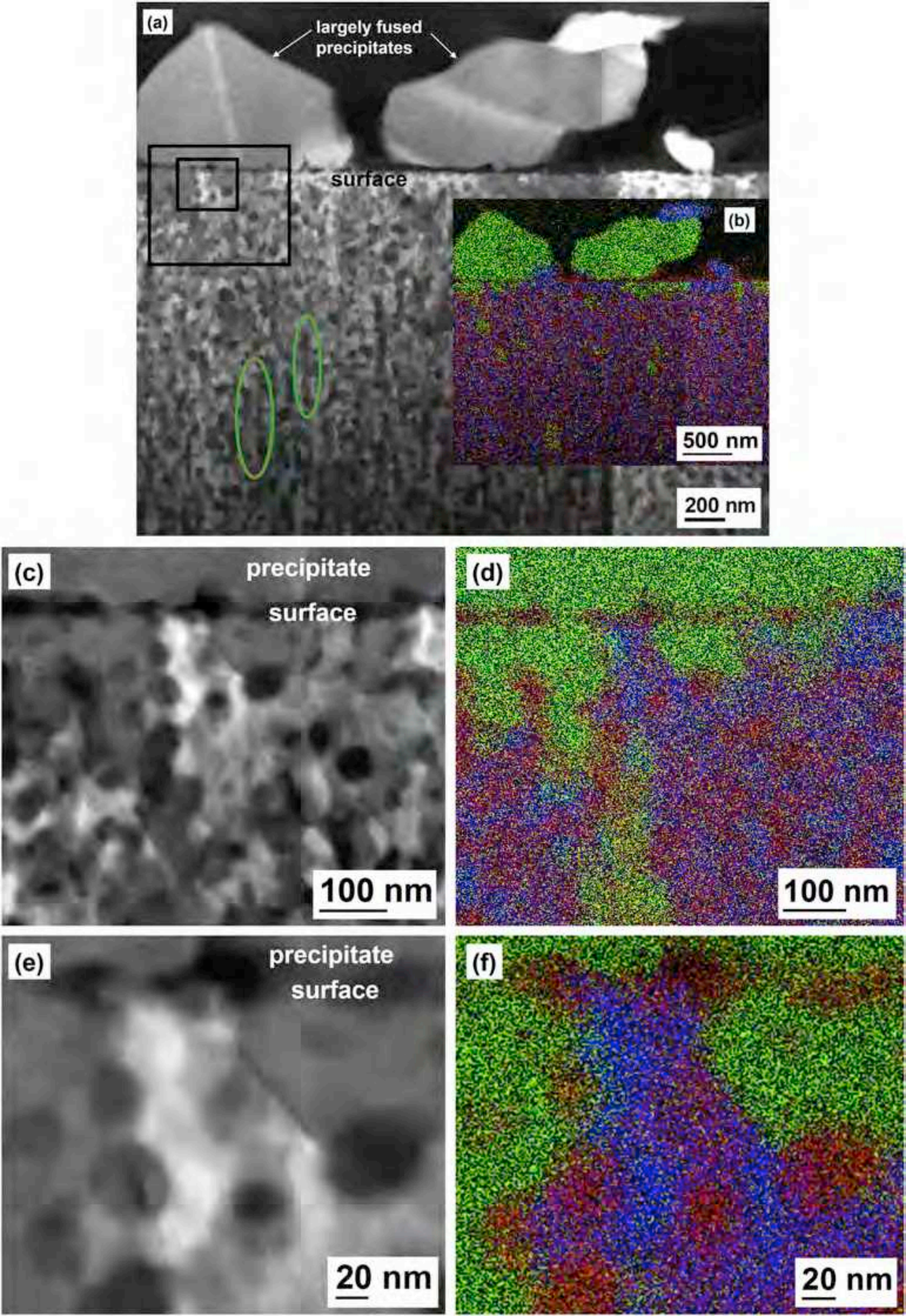
(a)
largely fused precipitates
surface
(b)
500 nm
200 nm
(c)
precipitate
surface
100 nm
(d)
100 nm
(e)
precipitate
surface
20 nm
(f)
20 nm